

Photocurrent measurements of supercollision cooling in graphene

Matt W. Graham^{1,2}, Su-Fei Shi^{1,2}, Daniel C. Ralph^{1,2}, Jiwoong Park^{1,3}, Paul L. McEuen^{1,2}

1. Kavli Institute at Cornell for Nanoscale Science, Ithaca, NY 14853, USA

2. Laboratory for Atomic and Solid State Physics, Cornell University

3. Department of Chemistry and Chemical Biology, Cornell University

S.1.1: Graphene photodetector device transport properties

Centrally located Dirac points were achieved for the vast majority of our devices by meticulously cleaning the CVD graphene. In particular, after etching the copper away we put the PMMA/graphene thin film through multiple washings with 18 MΩ DI water. We further leave it in DI water overnight so that absorbed residue from the etchant will diffuse away. We then performed multiple washing again before finally transferring the graphene/PMMA onto the silicon chip. We further get rid of PMMA by first immersing the graphene/PMMA in Anisole and then Dichromethane solution.

Supplemental Fig. S1a plots the graphene photodetector device conductance ($\times 100 \mu\text{S}$) across the source-drain electrodes as a function of top gate (TG) and back gate (BG) potentials at a base lattice temperature of $T_l = 10 \text{ K}$. A small source-drain bias was applied to define the directional flow. Two dips in the conductance are seen as the BG voltage is scanned. The vertically aligned blue region corresponds to the Dirac point with respect to the back gate, and the tilted blue region to the Dirac point of the top gate. The first dip occurring near $V_{BG} \approx 0 \text{ V}$ is the Dirac point of the graphene located away from the local top gate, and originates exclusively from the global back gate coupling. The second dip is also a

graphene Dirac point, but depends strongly on the applied top gate voltage according to $V_{TG} - V_{TG}^{\text{Dirac}} = \frac{C_{TG}}{C_{BG}} (V_{TG} - V_{BG}^{\text{Dirac}})$,

where C_{TG} and C_{BG} are the gate capacitances. We calculate a mean mobility of $8,000 \text{ cm}^2 \text{ V}^{-1} \text{ s}^{-1}$ for our graphene photodetectors.

A SEM image of a graphene photodetector device is shown in Fig. S1b. The high quality of the single-layer graphene was optically confirmed by point-Raman and transient absorption spectroscopy.

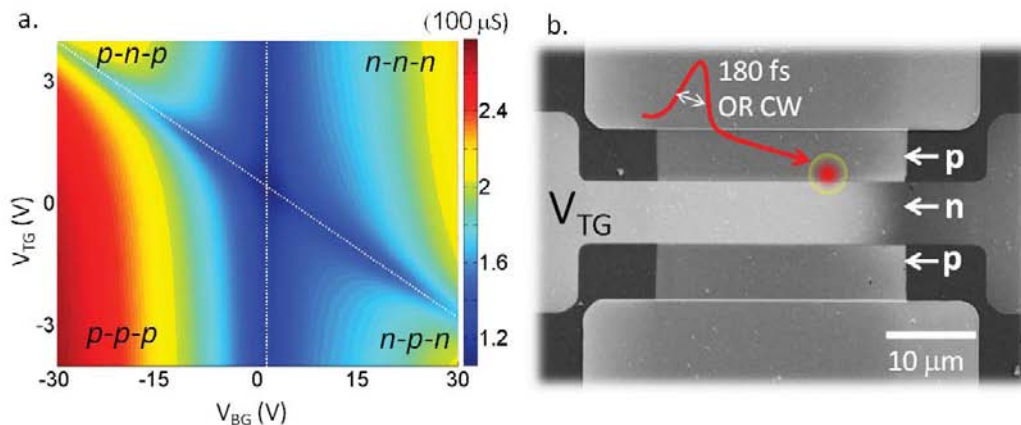


Figure S1: (a) Device conductance map, plotted as a function of the tunable electrostatic gates (top gate V_{TG} ; global back gate V_{BG}). Four distinct regions are observed as the gate voltages are tuned. (b) SEM image of device. Single-layer graphene is patterned to $20 \times 30 \mu\text{m}$. Device is illuminated by a $1.5 \mu\text{m}$ CW or pulsed laser at 1.25 eV .

S.1.2: Device photocurrent (PC) properties (CW illumination)

To complement the pulsed excitation data presented in Fig. 2b, we show in Fig. S2 the spatial and gate-dependent PC maps under CW excitation (1.25 eV). As with the pulsed excitation case, we observe a clear double-sign reversal in PC generated for a monotonic top gate scan (see Figs. S2b and c). This double-sign reversal has been shown to be a hallmark of PC generation by a photothermal hot electron carrier response.^{1,2} Using this justification, we can apply the photothermal current generation to extract the electron temperatures for both the CW and pulsed excitation cases.¹

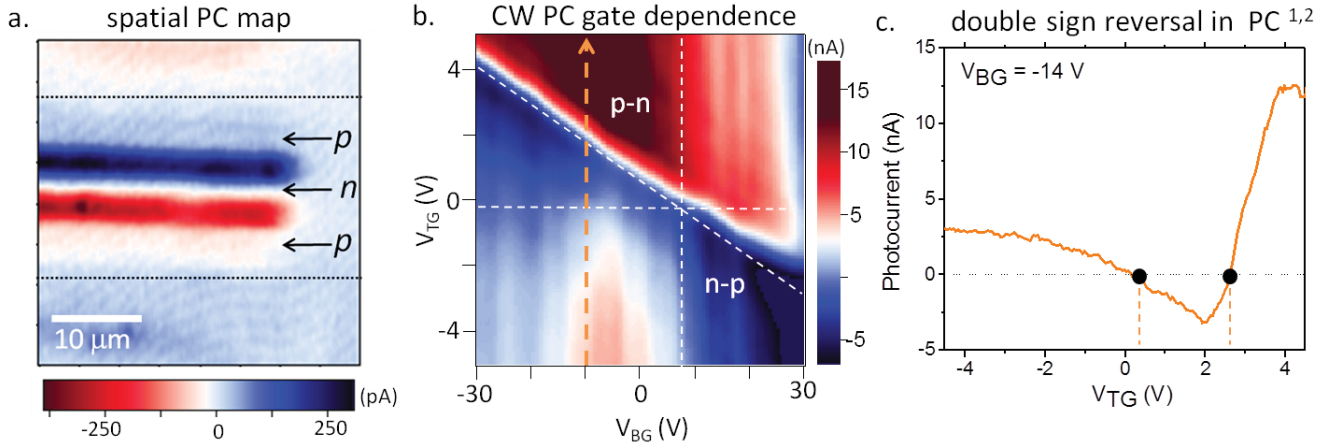


Figure S2: (a) Spatial photocurrent map. Maximal photocurrent is generated at the graphene p-n (red) and n-p (blue) junction regions. (b) CW photocurrent map at 1.25 eV excitation. The amplitude of the PC collected is measured as a function of the electrostatic gate potentials. We calculate a maximum electrostatic doping of 0.14 eV for the voltages applied. (c) Line trace of PC generated as function of top gate voltage for a constant back gate voltage of -14 V. A double sign-change in photocurrent is observed for a monotonic gate voltage sweep, in accord with predictions for PC generation by the photothermal hot carrier effect.^{1,2}

The carrier density varies strongly near the charge neutrality region of the p-n junction, but it is relatively constant on each side of the junction away from the charge neutrality region, where the density is determined by the applied gate voltages. Since the dielectric spacing separating our applied gates is small (at 200 nm and 10 nm) compared to our 1.5 μm beam diameter we conclude that the charge neutrality region of our p-n junctions is much smaller than the optically excited region. Consequently, the vast majority of carriers are created in an environment with doping comparable to that of the applied gates.

S.2: Quantitative analysis of photocurrent generated using one- and two-pulse excitation techniques

Hot electron relaxation kinetics at graphene p-n junctions occur on the femto- and picosecond time-scale, too fast to measure with direct electronic detection.³ To overcome this limitation, we use a two-pulse correlation technique whose temporal resolution is only limited by the laser pulse duration. We collect the photocurrent generated (I_{1p}) when an incident photon flux (F) excites hot electronic carriers in a graphene p-n or n-p junction (see Fig. S2). Incident laser pulses have 180 fs FWHM duration at pulse repetition rate of $f = 76$ MHz. The average photocurrent detected under pulsed conditions is $I_{1p} = Q_1 f$, and is directly related to the average number of e - h pairs collected (Q_1 / e) per pulse.

S.2.1: Pulsed Photocurrent Charge Collection, $Q_1(t)$

A pulsed photocurrent measurement for the average charge collected (Q_1) derives from an inherent detection integration $Q_1 = \int i(t) dt$ (Equation (5)) over the number of e - h pairs detected over a time interval dt . From our data in Fig. 4b, we showed the supercollision (SC) rate law $dT(t)/dt = -(A/\alpha) \cdot T^2(t)$ generates the functional form that best fits our data at taken low base-lattice temperatures. To relate this cooling rate to the photocurrent generated, we first solve for $T(t)$ under the initial condition that $T(0) = T_o$, obtaining:

$$T(t, T_o) = \frac{T_o}{1 + AT_o t / \alpha} \quad (\text{S1})$$

where T_o is the initial electron temperature. In the photothermal hot carrier model, the instantaneous thermoelectric current can be expressed as $i(t) = \beta T(t) (T(t) - T_f) \approx \beta T^2(t)$ when $T(t) \gg T_f$. Combining equation (S1) and (3) we can express the cumulative charge collected after a delay time t_d as:

$$Q_1(t_d) = \int_0^{t_d} \frac{\beta T_o^2}{(1 + AT_o t/\alpha)^2} dt = \beta \tau_o T_o^2 \left(1 - \frac{1}{1 + t_d/\tau_o} \right), \text{ where } \tau_o \equiv \frac{\alpha}{A} T_o \quad (\text{S2}).$$

We can further take the long-time limit ($t_d \rightarrow \infty$) to obtain $Q_1(\infty) = \beta \tau_o T_o^2$ (Eq. 5).

In the above model we assumed hot electron cooling processes at the p-n junction are the driving force producing the observed nonlinear kinetic photocurrent response. However, electrons also radiate spatially, dissipating heat. These contributions to the transient signal decay can be safely neglected if their kinetic rate contribution is linear, or if these transport processes occur on long time scales compared with the carrier cooling time scale (τ_o) at the p-n junction. The diffusive motion of the hot electrons is slow compared to timescales observed in the transient PC response. This can be seen by calculating characteristic diffusion length $l = \sqrt{D\tau_o}$, where D is the carrier diffusivity. On the ~10-20 ps timescale relevant for our observed kinetics, we find the hot carrier diffusion length to be substantially smaller than the ~1.5 μm spatial extent of our optical excitation.

S.2.2: Two-Pulse Photocurrent Response Function, $\Delta Q_{12}(t)$

We next derive an analytic expression for our transient photocurrent (TPC) response ($\Delta Q_{12}(t)$) plotted in Fig. 4. Starting with two collinear laser pulses of equal intensity separated by a time delay t_d (see Fig. 2c), each pulse independently generates a total charge Q_1 with an associated initial electron temperature T_o as outlined in equation (S2). We define the TPC response function, $\Delta Q_{12}(t_d) \equiv 2Q_1(\infty) - Q_{12}(t)$ as the difference between the total charge generated by two well-separated pulses (i.e., $2Q_1(\infty)$) and the total charged generated ($Q_{12}(t_d)$) when they are separated by a delay time t_d .

Using equation (5) we can integrate piecewise the total charge collected, using the two separate time regions which correspond to the one and two-pulse current-generation time-periods respectively. Prior to the arrival of the second pulse, we generate a charge $Q_1(t_d) = \beta \int_0^{t_d} T(t, T_o)^2 dt$ (equation (S2)). Upon arrival of the second pulse at time $t = t_d$, we will collect a charge $Q_2(t_d) = \beta \int_{t_d}^{\infty} \left[T(t - t_d, \sqrt{T_o^2 + T(t_d)^2}) \right]^2 dt$. The total response function is the difference between the charge generated by two independent pulses and the charge generated by two pulses at delay time t_d , i.e.

$$\Delta Q_{12}(t_d) = 2Q_1(\infty) - \beta \int_0^{t_d} T(t, T_o) (T(t, T_o) - T_l) dt + \beta \int_{t_d}^{\infty} \left[T(t - t_d, \sqrt{T_o^2 + T(t_d)^2}) \right] dt. \quad (\text{S3})$$

In the limit where $T(t) \gg T_l$ we can analytically solve for the transient response using equations (S1-S2),

$$\Delta Q_{12}(t_d) = 2\beta \tau_o T_o^2 - \beta \left(\int_0^{t_d} \frac{T_o^2}{(1 + t/\tau_o)^2} dt + \int_{t_d}^{\infty} \frac{T_o^2 (1 + (1 + t_d/\tau_o)^{-2})}{\left(1 + \sqrt{1 + (1 + t_d/\tau_o)^{-2}} \frac{(t - t_d)}{\tau_o} \right)^2} dt \right) \quad (\text{S4})$$

$$\Delta Q_{12}(t_d) = \beta \tau_o T_o^2 \left(1 + \frac{1}{1 + t_d/\tau_o} - \sqrt{1 + (1 + t_d/\tau_o)^{-2}} \right) \quad (\text{S5})$$

As shown by the fits in Fig. 4b, the above analytic form models the TPC time-dependent decay with only two fit parameters (i.e. an amplitude $Q_1 = \beta \tau_o T_o^2$ and a time constant $\tau_o = \alpha/AT_o$). Near time-zero, the charge collected will be reduced by

$\Delta Q_{12}(t \rightarrow 0) = (2 - \sqrt{2}) \beta \tau_o T_o^2$, giving rise to the observed transient PC dip in Fig. 4a. Conversely, at longer delay times compared to τ_o we get $\sqrt{1 + (1 + t_d/\tau_o)^{-2}} \approx 1$. Under these approximations equation (S5) predicts $\Delta Q_{12}(t_d)$ scales

inversely with delay time. This simple approximate form captures the general behavior of our low-temperature TPC results. This is shown in Fig. 4b, in which $\Delta Q_{12}(t_d)$ kinetic decay is closely linearized when plotted on an reciprocal axis scale.

S.3: Transient PC response, $\Delta Q_{12}(t, T_l)$ at for arbitrary lattice temperatures

At arbitrary temperatures, the lattice temperature cannot be neglected and the full supercollision model must be used. Using the SC model⁴ for doped graphene we obtain:

$$\frac{dT(t)}{dt} = -\frac{A}{\alpha} \frac{(T(t)^3 - T_l^3)}{T(t)} \quad (\text{S6}).$$

We solve the above differential equation analytically for a given lattice temperature. The initial condition must take into account both the electronic energy deposited by the laser pulse, and the existing energy in the lattice. The initial temperature is expressed as $T(0) = T_o = \sqrt{T_{eo}^2 + T_l^2}$ (i.e. adding the energies $E = 1/2 \alpha T^2$). Our initial condition is $T_o = \sqrt{T_{eo}^2 + T_l^2}$ where T_{eo} is 1250 K for the incident photon flux used (see Fig. 3b(*inset*)). Solving the SC model for the transient temperature decay give the following results:

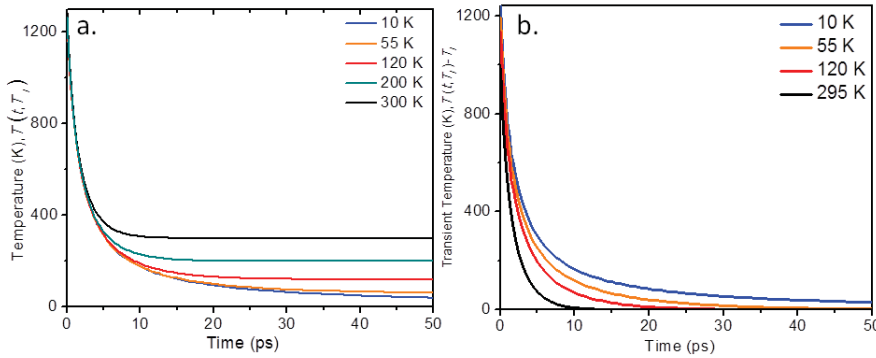


Figure S3: (a) SC model prediction for transient electron temperature decay at selected lattice temperatures. The result depends strongly on the base lattice temperature. At long times, $T(t, T_l) = T_l$, as required. (b) The photocurrent response is driven by the temperature gradient $T(t, T_l) - T_l$ plotted (shown on log scale in Fig. 1). The solution for the transient temperature is qualitatively analogous to the observed transient PC response (fig. 5) and is explicitly related through equation (S7).

In Figure 5, we further use the above solutions for $T(t, T_l)$ to numerically calculate the corresponding TPC response $\Delta Q_{12}(t_d)$ using the generalized form of equation (S3):

$$\Delta Q_{12}(t_d) = 2 Q_1(\infty) - \beta \int_0^{t_d} T(t, T_o) (T(t, T_o) - T_l) dt + \beta \int_t^\infty T\left(t - t_d, \sqrt{T_o^2 + T(t_d)^2}\right) \cdot \left(T\left(t - t_d, \sqrt{T_o^2 + T(t_d)^2}\right) - T_l\right) dt. \quad (\text{S7}).$$

In a typical pulsed measurement the initial electronic temperature (T_{eo}) is in the 600 to 1300 K range, and hence $T(t) \gg T_l$ except at very long delay times. In this regime we can approximately set $T_l = 0$ and obtain the approximate solution given in equation (S5). Additionally, it is helpful to consider the behavior in the cross-over regime where $T_l \approx T(t)$. Rearranging equation (S6) and Taylor expanding to second order, we obtain:

$$\frac{d(T/T_l)^2}{dt} = \frac{-2A \cdot T_l}{\alpha} \cdot \left(\left(\frac{T}{T_l} \right)^3 - 1 \right) \approx \frac{-2A \cdot T_l}{\alpha} \left(3 \left(\frac{T}{T_l} \right)^2 - 3 \left(\frac{T}{T_l} \right) \right) \Rightarrow \frac{dT}{dt} \approx \frac{-3A}{\alpha} \cdot T_l \cdot (T - T_l) \quad (\text{S8})$$

Solving (S8) we obtain an exponentially decaying temperature $T_{\text{exp}}(t) = T_l + (T_o - T_l) \cdot \exp\left(\frac{-3A T_l t}{\alpha}\right)$, as plotted in Fig. 1 for $T_l = 295$ K. Substituting (S8) into equation (S3) for the TPC response, the SC model predicts that $\Delta Q_{12}(t_d)$ is

exponential in nature when $T_l \approx T(t)$ (as observed experimentally in Fig. 5).

S.4: Determination of β

Extracting from PC power dependence:

Using a SC model for cooling and a thermoelectric mechanism for current production¹, we can extract β from our CW excitation PC data. In the CW limit, $H_{SC} = P_{in}$ giving $P_{in} = A(T^3 - T_l^3)$ or a temperature, $T = \sqrt[3]{P_{in}/A + T_l^3}$. The resulting PC generated is then simply, $I_{CW}(P_{in}) = \beta T(T - T_l) = \beta \sqrt[3]{P_{in}/A + T_l^3} (\sqrt[3]{P_{in}/A + T_l^3} - T_l)$. Consequently by fitting a curve of photocurrent vs. power (for a given T_l), the value of β may analytically extracted.

Approximate solutions can be also expressed in following two limits:

1) for $T \gg T_l$, $P_{in} = AT^3$

2) for $T \approx T_l$ we Taylor expand to obtain, $P_{in} = AT_l^3 \left(\left(\frac{T}{T_l} \right)^3 - 1 \right) \approx 3AT_l^2(T - T_l) \Rightarrow P_{in} \approx 3AT_l^2(T - T_l)$.

We now estimate a cross-over temperature (T_c) by equating limits #1 and #2 above to obtain,

$T_c = 3(T_c - T_l)$ or $T_c = 3/2 T_l$. In Fig. 3a (inset) we see that indeed $T_c \approx 15$ K as predicted for a 10 K base temperature. We can further use the above with photothermal model (Eq. (3)) to define a corresponding cross-over current (I_c) which occurs at:

$$I_c = \beta T_c(T_c - T_l) \approx \frac{\beta T_c^2}{3} = \frac{3}{4} \beta T_l^2 \quad (S9)$$

This provides a direct way to extract β i.e., $\beta = 4/3 \frac{I_c}{T_l^2}$. Using figures 3a and c (upper panel) we extrapolate the values of the I_c and calculate a mean β of **1.1 pA/K²**.

Using a *different graphene device* of the same dimensions, we repeat our experimental determination of β in Figure 3, by plotting the PC amplitude dependence on incident power(P) for selected base lattice temperatures below.

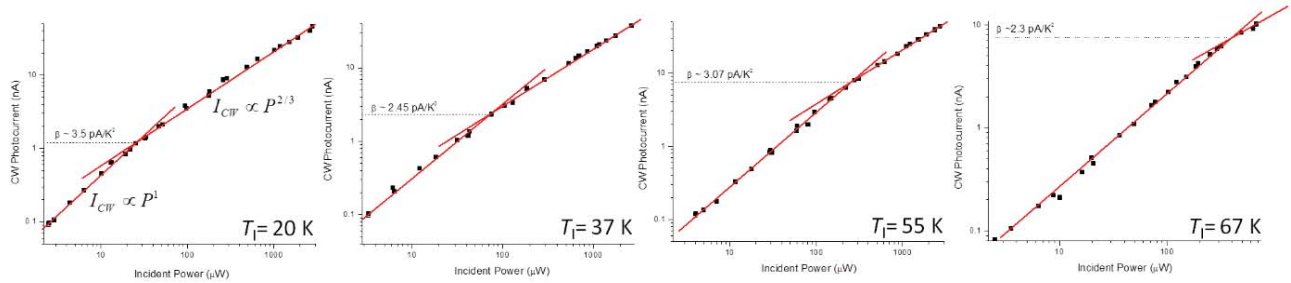


Figure S4: Log-log plots of photocurrent vs. incident CW power for selected lattice temperatures. The values of β can be estimated from the cross-over current (I_c), where the scaling changes from P^1 to $P^{2/3}$.

When plotted on a log-log scale above we observe a distinct “cross-over” from a linear to $P^{2/3}$ dependence. Such a cross-over is predicted by the SC analytic form $I_{CW}(P_{in}) = \beta T(T - T_l) = \beta \sqrt[3]{P_{in}/A + T_l^3} (\sqrt[3]{P_{in}/A + T_l^3} - T_l)$, in the two relevant limits of $T \gg T_l$ and $T \approx T_l$.

As the lattice temperature is raised, the value of the observed cross-over temperature is roughly proportional to square of the lattice temperature. This is in accord with the predicted form $I_c = 3/4 \beta T_l^2$. Using this we extract a mean 2.8 ± 0.6 pA/K² for this device. Considering device-dependent differences, this compares favorably with the one presented in Fig. 3c, that gives ~ 1.1 pA/K².

Estimation from transport measurements:

We can get a rough estimate of the value of β using the transport measurements on our graphene devices. From the Mott formula we can express the Seebeck coefficient (S), in terms of the graphene resistance (R) as¹,

$$S = \frac{\pi^2 k_B^2 T}{3e} \frac{1}{R} \frac{dR}{d\mu}$$

The desired parameter β is directly related to the Seebeck coefficient, but must be scaled by the laser spot diameter ($\lambda=1.5 \mu\text{m}$) vs. junction width ($W=20$) to give us a value relevant for our experimental conditions (see Fig. S5 (inset)).^{1,5} Using the above definition for S we get:

$$\beta \approx \frac{S}{TR} \frac{d}{W} = \frac{\pi^2 k_B^2}{3e} \frac{1}{R^2} \frac{d}{W} \frac{dR}{dV_G} \frac{dV_G}{d\mu}$$

The dependence of the Fermi energy (μ) on the capacitive gate coupling can be readily derived from the graphene density of

states to be: $\mu(V_G) = \hbar v_F \sqrt{\frac{\pi \epsilon_r \epsilon_0 V_G}{ed}}$, where ϵ_r is the dielectric constant, ϵ_0 the permittivity and d is the thickness of the

dielectric medium. Using a back gate silicon oxide thickness of 200 nm we get $\mu(V_G) \approx 0.032 \sqrt{V_G}$ or

$$\frac{dV_G}{d\mu} \approx 1950 \left[\frac{V}{eV} \right] \mu.$$

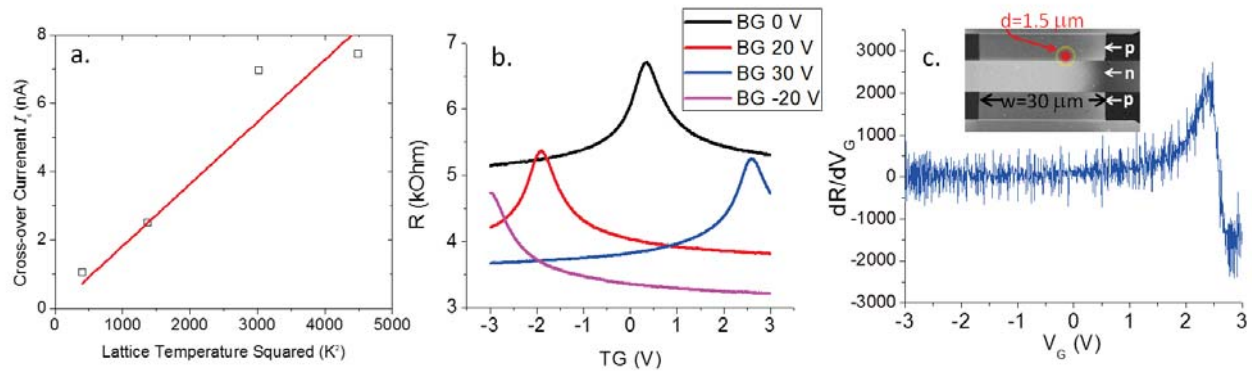


Figure S5: (a) The current at which the power dependence becomes nonlinear ($P^{2/3}$) increases with T_1^2 , where $\beta \approx 4/3 I_c T_1^2$. (b) Resistance vs. top gate voltage sweep for various back gate voltages. (c) The derivative of the BG=30 V curve at the $V_G = -2$ V position of the top gate has a mean value of $dR/dV_G = 15 \frac{\Omega}{V}$. (inset) The ratio $d/W = 1.5/30$ is applied to scale the bulk transport measurement down to active area of our laser spot shown.

Using the values relevant to our p-n junction (30 V back gate, -2 V top gate, 0.14 eV doping) we obtain:

$$\beta = \frac{\pi^2 k_B^2}{3e} \frac{1}{(3600 \Omega)^2} \cdot 15 \left[\frac{\Omega}{V} \right] \cdot 280 \left[\frac{V}{eV} \right] \left(\frac{1.5}{30} \right) \approx 0.5 \text{ pA/K}^2$$

This very crude estimate using just transport measurements is similar to the experimental values extracted above at our exact experimental conditions using CW photocurrent measurements.

S.5: Relating the pulsed and CW photocurrent response

To relate the wildly disparate magnitude of CW and pulse excitation PC collected, we first examine their power dependences individually. Rearranging equations (4) and (5) we obtain:

$$\text{CW: } P_{\text{in}} = A \left(\frac{I_{\text{CW}}}{\beta} \right)^{\frac{3}{2}}$$

$$\text{Pulsed: } Q_1 f \equiv I_{1p} = \beta f \left(\frac{\alpha}{A} \right) T_o = \beta f \left(\frac{\alpha}{A} \right) \sqrt{\frac{2 F_{\text{in}}}{\alpha}} \quad \text{OR} \quad F_{\text{in}} f = \frac{1}{2 \alpha f} \left(\frac{I_{1p} A}{\beta} \right)^2.$$

We can now evaluate the PC ratio I_{1p}/I_{CW} by setting the CW and pulsed incident power equal ($P_{\text{in}} = F_{\text{in}} f$), obtaining

$$A \left(\frac{I_{CW}}{\beta} \right)^{\frac{3}{2}} = \frac{1}{2 \alpha f} \left(\frac{I_{1p} A}{\beta} \right)^2 \Rightarrow I_{1p}^2 = I_{CW}^{3/2} \sqrt{4 f^2 Q_1 \tau_o}. \quad (S10)$$

Furthermore, we note that $Q_1 = I_{1p}/f$ giving $I_{1p}^{3/2} = I_{CW}^{3/2} \sqrt{4 f \tau_o}$ or equivalently $I_{1p}/I_{CW} = \sqrt[3]{4 f \tau_o}$.

From our time-resolved PC we extracted τ_o to be $1.8 \times 10^{-9} [\text{K} \cdot \text{s}] T_o^{-1}$. Consequently, SC model predicts a CW to pulsed

PC ratio giving by, $\frac{I_{CW}}{I_{1p}} = \frac{1}{\sqrt[3]{4 f \tau_o}} \approx 1 / \sqrt[3]{4 \cdot 76.1 \times 10^6 [\text{s}^{-1}] \cdot 1.8 \times 10^{-9} [\text{K} \cdot \text{s}] \cdot T_o^{-1}} \approx 1.2 \sqrt[3]{T_o}$.

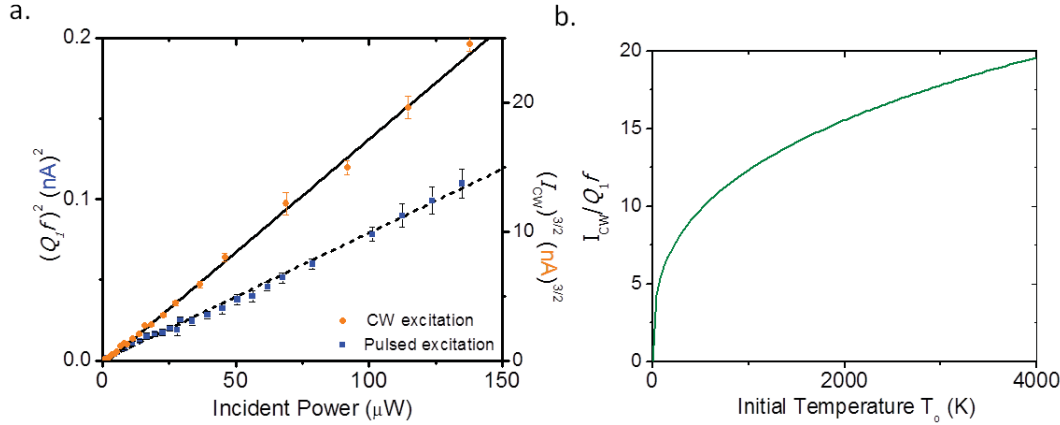


Figure S6: (a) CW and pulsed PC power dependence at $T_l = 10$ K are closely linear (black line fits) when plotted as $I_{CW}^{3/2}$ and $(Q_1 f)^2$. The absolute magnitude of PC collected differs by factor of ~ 10 to 20, with the difference getting larger as incident power is increased. **(b)** Plot of the predicted CW to pulsed PC ratio for a given initial temperature of the the hot electron gas (for a pulsed excitation measurement).

Figure 3b shows the range of initial temperatures, T_o investigated is ~ 300 to 3500 K. For this range, our SC model theory predicts the I_{CW}/I_{1p} ratio will vary from ~ 8 to 18 (see Fig. S6b). This prediction is in excellent accord with the ~ 10 to 20 experimental ratio observed, and provides an independent check that CW and pulsed experiments can be explained by the same fundamental underlying physics of SC hot electron cooling.

S.6: Disorder dependence of hot electron cooling rate

We find selectively doping (up to ~ 0.14 eV) our graphene photodetector using our applied gates moderately changes our extracted hot electron cooling time (τ_o) by up to 35%. Even when the device is tuned to an asymmetrically doped n - n region, the data fits well to our simple transient photocurrent response function (equation S5) with near identical hot electron cooling timescales as the p - n junction regions (see Fig. S7a). In Fig. S7b, we plot the measured device conductance (G) and τ_o as function of the applied back gate voltage. Comparing the two curves, we that observe $\tau_o \propto G$.

To check if the dependence observed in Fig. S7 below is consistent with the supercollision mechanism put forward in the manuscript we compare against the SC model prediction, $A/\alpha \propto E_F/k_F l$.⁴ The mean free ($k_F l$) path can be approximated in terms of the conductivity(σ) as $k_F l = \sigma h / 2e^2$, giving $A/\alpha \propto E_F/\sigma$. Using the definition of the hot electron cooling time, the SC model predicts:

$$\tau_o = \left(\frac{A}{\alpha T_o} \right)^{-1} \propto \left(\frac{E_F}{k_F l \sqrt{\frac{2F}{\alpha(E_F)}}} \right)^{-1} \propto \frac{\sigma}{\sqrt{E_F}}$$

Away from the Dirac point in graphene $E_F \propto \sqrt{n}$, giving a prediction $\tau_o \propto G/\sqrt{n}$. Close the Dirac point, the graphene junction breaks up into effectively doped “puddles” of electron and holes, and the predicted dependence is non-trivial, and not investigated here. The data in Fig. S7 qualitatively agrees with the SC prediction on $k_F l$. Away from the Dirac point we

predict $\tau_o \propto G/\sqrt[4]{n}$, and we indeed observe $\tau_o \propto G$.

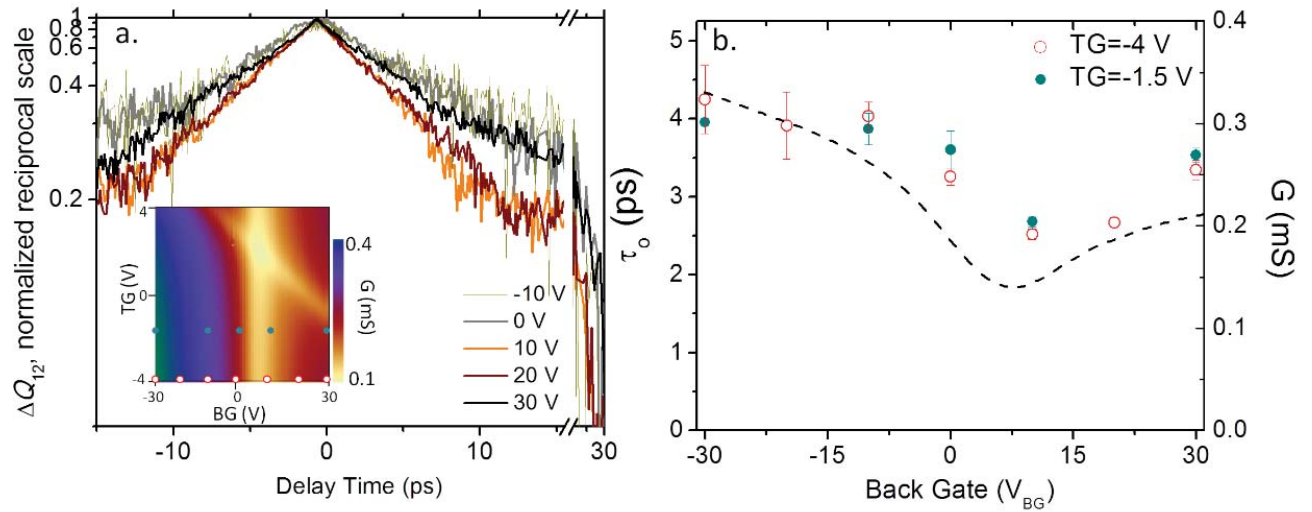


Figure S7- (a) Normalized transient photocurrent as function of back gate shown for constant top gate voltage of -4 V. Data is plotted on reciprocal scale, and shows the cool rate accelerates as the Dirac point is crossed. (inset) Associated conductance map of the device showing where the hot electron cooling kinetics were measured (circles). (b) Extracted hot electron cooling times as a function of back gate voltage, and the associated conductance (for -4V top gate).

S.7: References

- [1] N. M. Gabor, J. C. W. Song, Q. Ma, N. L. Nair, T. Taychatanapat, K. Watanabe, T. Taniguchi, L. S. Levitov, and P. Jarillo-Herrero, *Science*, 2011, 334(6056), 648 –652.
- [2] J. C. Song, M. S. Rudner, C. M. Marcus, and L. S. Levitov, *Nano Lett.*, 2011, 11(11), 4688–4692.
- [3] M. Breusing, C. Ropers, and T. Elsaesser, *Phys Rev Lett*, 2009, 102(8), 086809.
- [4] J. C. W. Song, M. Y. Reizer, and L. S. Levitov, *arXiv:1111.4678*, 2011.
- [5] J. C. W Song and L. S Levitov *arXiv:1112.5654 [cond-mat.mes-hall]*.